8 ABERRATION ANALYSIS AND THIRD ORDER THEORY

8.1 SIGNIFICANCE OF RAY TRACE DATA

8.1.1 First order system.

8.1.1.1 In Sections 5, 6, and 7, formulae and techniques were presented to enable the designer to set up a first order optical system. As an aid in arriving at a final first order solution, it is customary to trace two paraxial rays. One of these starts from an object point on the optical axis and heads toward the tentative edge of the entrance pupil. The other ray starts from an object point at the tentative edge of the field and heads toward the tentative center of the entrance pupil.

8.1.1.2 The data from these two rays may be used to determine the trace of any other paraxial ray through the system. The magnification, focal length, and chromatic aberration may be calculated. The planes of the paraxial image, entrance pupil, aperture stop, exit pupil, and field stop may be finally located, and the sizes of the pupils and stops can be finally determined. The f - number and fields of view can be calculated.

8.1.1.3 The calculation of the above characteristics of a first order solution has already been discussed. Additional calculations using paraxial ray trace data will be given later in this section where the aberrations of a system will be analyzed, and a third order theory will be developed which will provide understanding of the sources of image errors and suggest methods for correcting these errors.

8.1.2 Skew ray trace. After a first order system has been set up, skew and meridional rays are traced by the methods discussed in Section 5. This tracing of skew rays provides the basic method of investigating lens performance. The paraxial image and the entrance pupil furnish excellent reference planes which are used in the interpretation of non-paraxial ray trace data.

8.2 THE SPOT DIAGRAM

8.2.1 Representation of ray trace data. One way to make a graphical summation of ray trace data is by means of a spot diagram. Such a diagram is a plot of the intersection coordinates in the reference planes of rays traced through the lens or system from a single object point. The two reference planes usually chosen are the entrance pupil plane and the paraxial image plane. The rays traced from the object point are usually chosen so as to form a uniform pattern of intersection with the entrance pupil plane while the resulting image is represented by the ray intersections in the paraxial image plane. Figures 8.1 (a) and 8.1 (b) show typical spot diagrams of this type for rays traced from an object point (object distance not specified) which lies in the YZ (meridional) plane at coordinates $X_o = 0$ and Y_o = an arbitrary value. Thus, the twelve spots at $X_1 = 0$ in Figure 8.1 (a) represent meridional rays; all others are skew rays. In Figure 8.1 (b), the meridional rays are at $X_k = 0$. There is a one to one correspondence between the spots in the two diagrams. In general, the spots at large values of X_1 correspond to the spots at large X_k. The Y_k axis is an axis of symmetry because the Y_1 axis is an axis of symmetry.

8.2.2 Ray distribution in the entrance pupil. The shape of the entrance pupil may be found with sufficient accuracy for most applications from paraxial ray tracing by the method described in Section 6. With automatic high speed computers it is possible to trace a regular grid of rays through the system. If any ray does not pass through every clear aperture the ray is rejected. With a computer program of this type, the shape of the vignetted aperture is automatically found as the boundary of the non-rejected rays.

8.2.3 Ray distribution in the image plane.

8.2.3.1 The spot diagram shown in Figure 8.1 (b) is extremely useful to a designer in evaluating a system. The diagram indicates how well the lens concentrates the energy from the object point into an image point. One can count the number of points in concentric circles in the image plane and obtain what is called an energy distribution curve. In Figure 8.1 (a) there are 192 points in the entrance pupil. If it is assumed that each point represents an equal amount of energy, a given point is equivalent to 1/192 of the total energy from the object point passing through the aperture. Now by drawing concentric circles around what appears to be the center of concentration of spots, and counting the number of spots within each circle one obtains the total energy as a function of (circular) image size. Figure 8.2 is a plot of percent energy versus image size for the spot diagram shown in Figure 8.1 (b). In a theoretically perfect geometrical image all the spots would be concentrated at a point. However, in the case of the image due to a perfect optical system, the geometrical image is only an approximation; the actual image formed would be larger than a point due to diffraction effects.

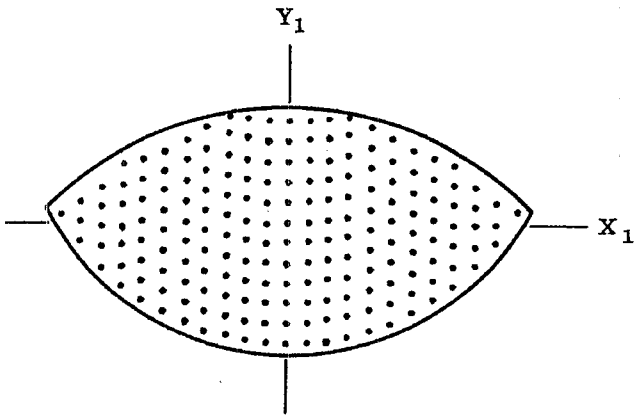

Figure 8.1 (a)- Spot diagram of rays passing through the entrance pupil.

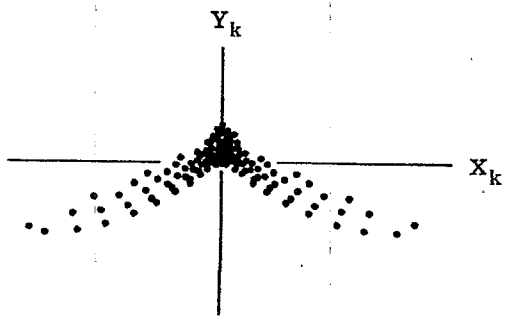

Figure 8.1 (b) - Spot diagram of rays incident on the paraxial image plane.

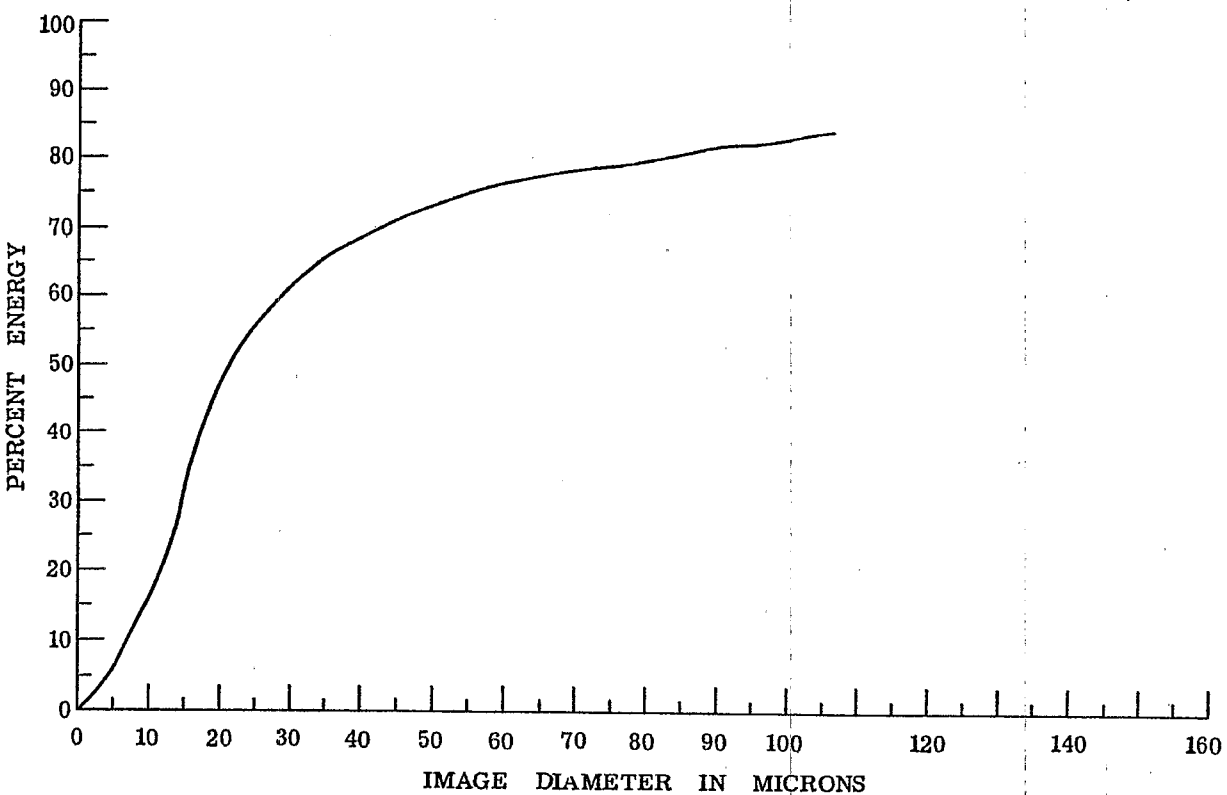

Figure 8.2- Energy distribution for the image shown in Figure 8.1 (b).

8.2.3.2 The spot diagram is useful in evaluating the image performance of a lens but it gives little insight to a designer as to why an image is spread out. In making a spot diagram, no attempt is usually made to identify each ray; therefore the designer usually has no means of visualizing what happens to the ray as it passes through the lens. Of course, it is perfectly possible to program the computer so that each ray in Figure 8.1 (b) is identified with a ray in Figure 8.1 (a), but with the large number of rays usually chosen for energy distribution representation, this would be unnecessarily complex. Instead, in order to understand the reason for image deformation, it is common practice to trace only a few selected rays through the aperture and plot the data in a different manner.

8.3 MERIDIONAL AND SKEW FANS

8.3.1 General method.

8.3.1.1 Instead of using spot diagrams and energy distribution functions, the ray trace data usually may be more conveniently analyzed by the method of meridional and skew ray fans. In using this method a common practice is to trace from a selected object point in the YZ plane, five to seven meridional rays (rays lying in the YZ plane) through the system. These rays, called the meridional ray fan, are chosen to intersect the vignetted entrance pupil in a nearly uniform spread, with upper and lower extremes (the rim rays) as close as possible to the respective vignetted pupil limits. See Figure 8.3. One of these rays is chosen to intersect the entrance pupil at $X_1 = 0$, $Y_1 = 0$ and thus, by definition, is the chief ray. The angle between the chief ray from the given object point and the optical axis is used to identify the meridional ray fan and its associated skew ray fan. The latter is constructed by tracing three to five rays from the same object point, which enter the vignetted entrance pupil at the intersection of the pupil and the XZ plane, i.e., at $Y_1 = 0$. Rays having positive X values only are needed since the object point lies in the meridional plane and the system is therefore symmetrical about the YZ plane. On the other hand, since the object point is not necessarily on the optical axis, rays above and below the Z axis are not symmetrical, so that rays must be traced having both positive and negative Y values at the entrance pupil plane.

8.3.1.2 Since they lie in a plane throughout their passage through the system, the behavior of the meridional rays can be well understood by making a plot of the coordinates of each ray intercept in the image plane (Y_k) versus the corresponding ray intercept in the entrance pupil plane (Y_1). This, in effect, is a similar but much more accurate presentation of the ray height data which could be obtained through graphical ray tracing.

8.3.1.3 Skew rays, on the other hand, do not usually remain in a single plane during their passage through the system. Thus, even though we have simplified the problem by choosing only those that intersect the entrance pupil plane on the X_1 axis ($Y_1 = 0$), they will normally have both X and Y coordinates in the image plane. Thus, for skew rays, it is necessary to make two types of plots: X_k versus X_1, and Y_k versus X_1. For perfect geometrical imagery, these plots would be straight lines of zero slope.

8.3.2 Illustrative example. In the following paragraphs, the arrangement and interpretation of these three curves will be discussed in detail. The example to be used will employ the same lens as shown in Table 6.7, except that in the table, the entrance pupil plane was not included, therefore surface 1 is the first lens surface. However, in the following discussions, surface 1 will be the entrance pupil plane, surface 2 the first lens surface, and so on. This is illustrated in Figure 8.4, which is drawn to scale from Table 6.7. The lens is a typical photographic Taylor triplet. The object surface for the lens is at infinity; the entrance pupil plane is located 2.2 cms to the right of the first surface of the lens. Rays representing fans of obliquities of 0°, 10°, 15°, and 20° have been traced into the system. (Note: with the object at infinity, the term "fan" is somewhat of a misnomer since all rays from a given object point are parallel, a situation which would not exist if the object were at a finite distance). The diagram shows the path of the extreme upper and lower rays for field angles of 10° and 20°. The upper rim ray at 0° is also shown; the lower is similar by symmetry. Notice how the upper and lower rays at 10° and 20° do not pass through the edge of the aperture stop. This is because the designer decided to vignette the oblique rays in order to eliminate some badly aberrated rays. The back focal length (BFL) is the distance between the last surface of the last element (surface 7) and the second focal point. Table 8.1 gives the numerical values for this lens.

8.4 USE OF THIRD ORDER THEORY IN ABERRATION ANALYSIS

8.4.1 Ray trace data. The numerical data used in the following discussions are the results of paraxial, meridional and skew ray traces for the lens shown in Table 8.1 and Figure 8.4. This lens, with very slightly different ν - number, was given in Tables 6.6 and 6.7.

8.4.2 Analysis of data. The curves of ray trace data will be plotted and analyzed in a manner that will be helpful to the designer trying to minimize the aberrations. The plots and analyses will make use of the third order theory to investigate the third order aberrations which, as explained in Section 5.11.3 are the first

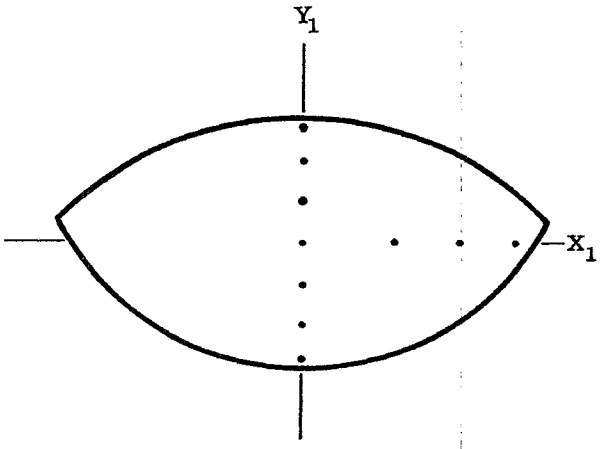

Figure 8.3 - Positions in the entrance pupil of selected meridional rays and skew rays used to analyze images.

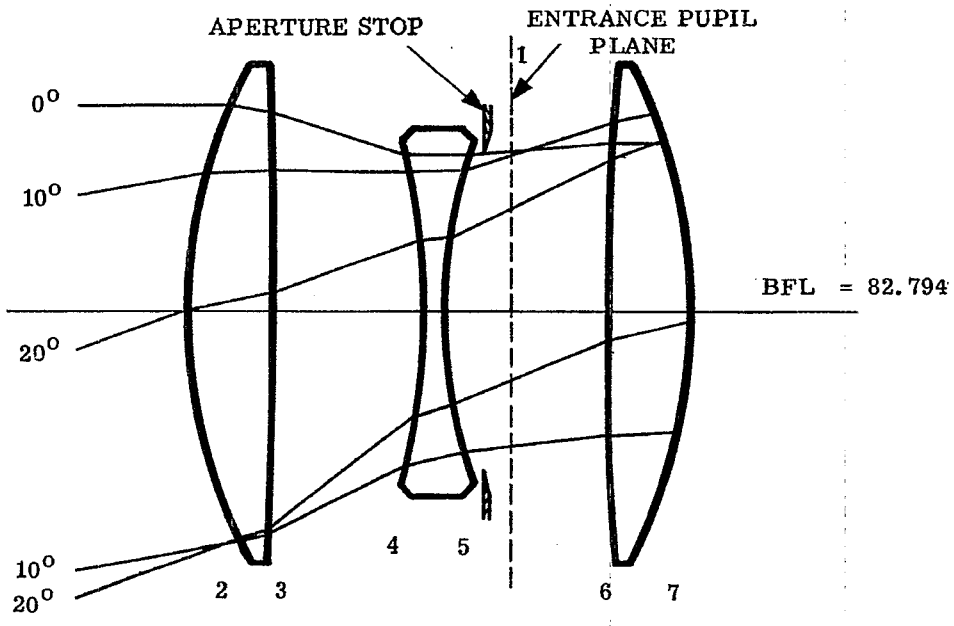

Figure 8.4 - Sample lens used for numerical analysis.

Surface	Radius	Thickness	n_D	ν-no.
2	39.55	6.0	1.620	60.3
3	-678.43	10.654	1.0	
4	-50.15	1.5	1.621	36.2
5	38.50	11.369	1.0	
6	197.43	6.0	1.620	60.3
7	-40.67			

Table 8.1 - Numerical values for lens in Figure 8.4. All lengths in millimeters. The numerical values are exact except for the radii. Exact curvatures are given in Table 8.2.

approximations to the aberrations. The method of plotting differs from that described in Section 8.3 in that only the essential information is shown. That is the difference in the paraxial plane intercepts for the chief ray and the other rays of the fans is plotted since it is this difference, or lack of coincidence, which the designer is trying to overcome.

8.5 THE 0° IMAGE IN D LIGHT

8.5.1 The 0° image polynomial.

8.5.1.1 The image of an axial object point at infinity is studied by tracing three meridional rays with $K_o = 0$, $L_o = 0$, $M_o = 1$ at values of $Y_1 = 1.5$, 1.0 and 0.5. For meridional rays from an axial object point, negative values of Y_j are symmetrical with the positive values. The results are plotted and encircled in Figure 8.5. The vertical scale is labelled $(Y_k - \overline{Y}_k)$. $\overline{Y}_k$ is the height of the chief ray $(\overline{Y}_1 = 0)$ on the final paraxial $(y_k = 0)$ image plane. For these axial rays $\overline{Y}_k = 0$. The circled points, connected by the full curve, can be fitted fairly accurately to a power series of the form

$$Y_k - \overline{Y}_k = b_1 Y_1 + b_3 Y_1^3 + b_5 Y_1^5 + O(7). \qquad (1)$$

The letters b_3, b_5, etc. are called the spherical aberration coefficients. The term $O(7)$ stands for all the terms of order 7 and above, as explained in Paragraph 5.5.2.3.

8.5.1.2 When ray data are plotted in this manner the slope of a line drawn between any two ray points on the curve is proportional to the longitudinal distance from the paraxial image plane to the plane where the two rays focus. That this is true, can be seen from Figure 8.6. This diagram shows two actual rays converging towards the image surface. The image surface, where the two rays focus, will be called the $k+1$ surface. The paraxial image plane is called the kth surface. By placing the paraxial image plane to the left of the intersections of the optical axis with rays (a) and (b), the two Y_k values are positive. Such a diagram would not represent the physical situation of a single converging lens, because for that case, the paraxial image plane is to the right of the intersection points of the optical axis with non-paraxial rays. The situation represented in Figure 8.6 could be attained, for example, by the forming of an image by a diverging system of an unaberrated, virtual object.

8.5.1.3 From the diagram we have

$$Y_{ka} = Y_{(k+1)a} - t_k \tan U_{(k-1)a}$$

and

$$Y_{kb} = Y_{(k+1)b} - t_k \tan U_{(k-1)b}.$$

Since $Y_{(k+1)a} = Y_{(k+1)b}$, subtraction gives

$$t_k = -\frac{Y_{ka} - Y_{kb}}{\tan U_{(k-1)a} - \tan U_{(k-1)b}}.$$

This equation and Figure 8.6 apply to two non-paraxial rays. It will be assumed that the following relation is a valid approximation for either of these rays; namely

$$\frac{Y_1}{\tan U_{k-1}} = \frac{y_1}{u_{k-1}}.$$

If these rays were paraxial, this relation would be exact; assuming it to hold approximately for non-paraxial rays, there results

$$\tan U_{(k-1)a} - \tan U_{(k-1)b} = \frac{Y_{1a}}{y_1 / u_{k-1}} - \frac{Y_{1b}}{y_1 / u_{k-1}},$$

and finally,

$$t_k = -\frac{y_1}{u_{k-1}} \left(\frac{Y_{kb} - Y_{ka}}{Y_{1b} - Y_{1a}} \right). \qquad (2)$$

When the object point is at infinity, then $-y_1 / u_{k-1} = f'$. Equation (2) is only an approximation for non-paraxial rays. But at worst it gives the order of magnitude of t_k; this is all that is needed for

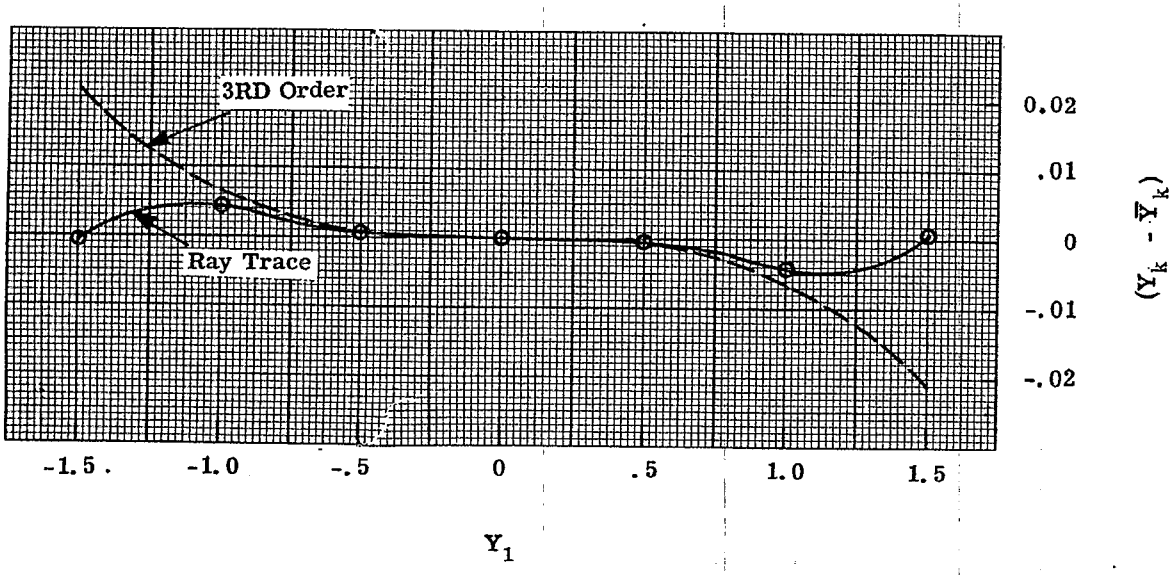

Figure 8.5 - Meridional ray plot at 0^o.

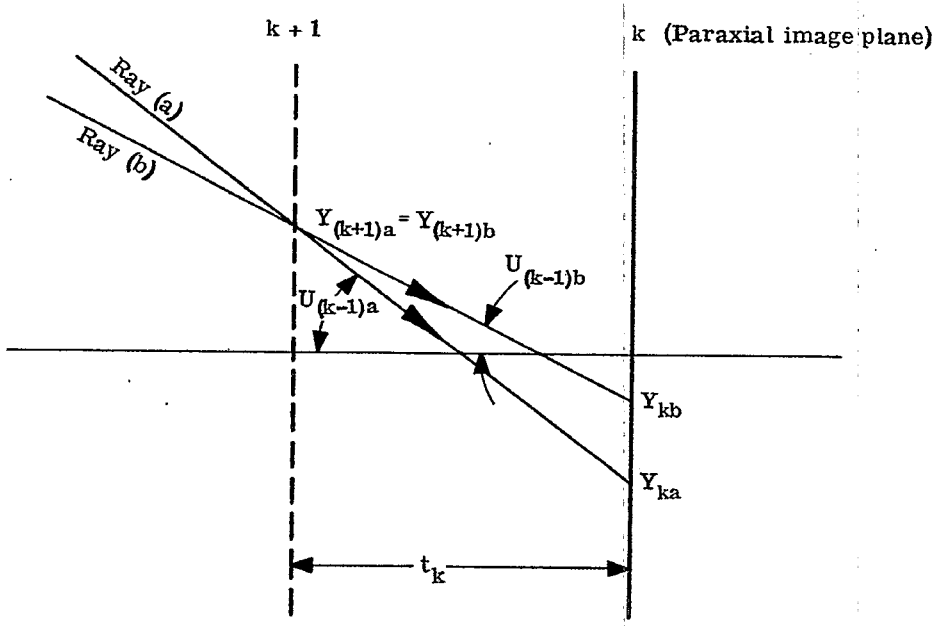

Figure 8.6 - Diagram illustrating shift of focus relationships.

third order design procedure.

8.5.1.4 Since the slope of the line connecting any two points on the $(Y_k - \overline{Y}_k)$ versus Y_1 curve is $\Delta Y_k / \Delta Y_1$, this slope is proportional to the distance from the paraxial image plane to the plane of focus for the two rays. As the two rays approach each other, the two points on the curve do likewise, and the slope of the chord approaches the slope of the curve. Hence the slope of the curve at any point is proportional to the distance from the paraxial image plane to the plane of focus for infinitely close rays. From ray trace data resulting in Figure 8.5, and from paraxial ray trace data giving y_1 / u_{k-1}, we are able to determine the shift (t_k) of the image plane from the paraxial image plane.

8.5.1.5 Now since the ray data shown in Figure 8.5 was obtained in the paraxial image plane the slope of the curve must be zero at $Y_1 = 0$. Therefore b_1 will be zero in Equation (1). The presence of a linear term indicated by a slope different from zero at $Y_1 = 0$, means that the paraxial rays are not focused in the final image plane upon which the ray heights are calculated. This linear term in Equation (1) can be eliminated by shifting the plane upon which the ray heights are calculated. When this has been done, so that the slope of the curve is zero at $Y_1 = 0$, and the linear term is absent, any further deviation, $(Y_k - \overline{Y}_k) \neq 0$, indicates the presence of spherical aberration. Therefore, the first approximation to the spherical aberration, written as $(Y_k - \overline{Y}_k)$, varies as the cube of the entrance pupil radius. This part of the spherical aberration, the third order spherical aberration, would vary with Y_1 as shown by the dashed line in Figure 8.5.

8.5.1.6 Because the slope of the line between any two points on the curve is proportional to the t_k for the two rays considered, Figure 8.5 shows that the rays traced at $Y_1 = 0.5$ and 1.0 are focused closer to the lens than the paraxial image plane, while the ray at $Y_1 = 1.5$ is focused almost exactly on the paraxial image plane. In this system, the third order coefficient, b_3, is negative and the lens is said to be undercorrected for the third order spherical aberration. It is called undercorrected spherical aberration because a single positive lens has spherical aberration of this sign. (See Paragraph 6.10.5.1). The coefficient, b_5, is called the fifth order coefficient. In this case it is positive because the full curve (Figure 8.5) is between the third order curve and $Y_k - \overline{Y}_k = 0$; hence the fifth order term [Equation (1)] has a sign opposite to that of the third order term. The fifth order coefficient is said to be overcorrected.

8.5.2 The third order aberration coefficient.

8.5.2.1 Now a truly remarkable feature of optical systems is that the coefficient, b_3, may be computed from axial paraxial ray data. This is done by calculating B_j, the third order spherical aberration surface contribution, at each surface in the optical system. Then,

$$b_3 = - \left[\frac{1}{2 (n_{k-1} \; u_{(k-1)}) \; y_1^3} \right] \sum_{j=1}^{j=k-1} B_j \; , *$$

where y_1 is the height of the axial paraxial ray in the entrance pupil plane and u_{k-1} is the final angle with the optical axis for this ray. Therefore, since $\overline{Y}_k = 0$ for 0° obliquity, the third order approximation for Y_k is,

$$_3Y_k = - \frac{\Sigma B}{2 (n_{k-1} \; u_{k-1})} \left(\frac{Y_1}{y_1} \right)^3 . \; ** \qquad (3)$$

8.5.2.2 B_j is calculated from the axial paraxial ray data for each surface with the following formulae

$$B = S i^2 , \qquad (4)$$

and

$$S = y \, n_{-1} \left(\frac{n_{-1}}{n} - 1 \right) (u + i) . \qquad (5)$$

In Table 8.2, B_j is calculated for each surface of the sample lens being studied. This is the same lens

* Up to this point in the text an attempt has been made to derive the equations, or to indicate specifically how they may be derived. This practice will no longer be followed; thus, equations may be presented without proof. To do otherwise would necessitate lengthy and complex departures from the main train of thought.

** In later sections the symbol Σ will be used to indicate the summation of all surface contributions. The proper summation limits will be eliminated.

Surface	Object	Entrance Pupil						Image	
	0	1	2	3	4	5	6	7	8	
c		0	0.25285	-0.01474	-0.19942	0.25973	0.05065	-0.24588	0	
t		-2.20000	0.60000	1.06541	0.15000	1.13691	0.60000	8.27937		
n	1.0000	1.00000	1.62000	1.00000	1.62100	1.00000	1.62000	1.00000		
$(n_{-1}/n)-1$			-0.382716	0.62000	-0.383097	0.62100	-0.382716	0.62000		
y		1.50000	1.50000	1.41291	1.14862	1.13883	1.22735	1.24192	0	
u	0	0	-0.145155	-0.24806	-0.065279	0.077866	0.02427	-0.15000		
i		0	0.37928	-0.16598	-0.47712	0.230508	0.14003	-0.281089		
u+i		0	0.23412	-0.41404	-0.54239	0.30837	0.16431	-0.43109		
B			-0.01933	-0.01619	0.05433	0.01878	-0.00151	-0.04249	Σ B = -0.00641	
$\bar{y}$		0	-0.80073	-0.61944	0.09189	-0.04712	0.49425	0.66486	$3Y_k$ = -0.02135	
$\bar{u}$	0.36397	0.36397	0.30216	0.49516	0.29845	0.47618	0.28436	0.35930	3.63966	
$\bar{i}$		0.36397	0.16150	0.31129	0.51348	0.28621	0.50121	0.12088		
F			-0.00823	0.03036	-0.05847	0.02332	-0.00542	0.01827	Σ F = -0.000170	
C			-0.00351	-0.05694	0.06293	0.02896	-0.01939	-0.00786	Σ C = -0.004200	
E			-0.01378	0.10994	-0.09223	0.07278	-0.09008	0.01544	Σ E = -0.002070	
P			-0.09677	-0.00564	0.07640	0.09950	-0.01938	-0.09410	Σ P = -0.04000	
dn/n		0	0.00635	0	0.01058	0	0.00635	0		
Δ (dn/n)			0.00635	-0.00635	0.01058	-0.01058	0.00635	-0.00635		
a			-0.00362	-0.00242	0.00580	0.00450	-0.00109	-0.00361	Σ a = -0.00040	
b			-0.00154	0.00452	-0.00624	0.00559	-0.00390	0.00154	Σ b = -0.000026	

Table 8.2 - Third order calculations on triplet lens in Figure 8.4.

illustrated in Table 6.7. The dotted curve in Figure 8.5 shows the third order curve as predicted by Equation (3). One notes that at $Y_1 = 1.5$, the dotted curve passes through the point $Y_k = -0.0214$. Notice also how the third order curve follows the true aberration curve very closely out to $Y_1 = 0.75$.

8.5.2.3 Returning to Equation (1) it follows that $b_3 = -0.0214/y_1^3 = -0.006341$. Since the actual ray traced at $Y_1 = 1.5$ strikes the final image plane at $Y_k = 0$ it is possible to compute that $b_5 = 0.002818$ if it is assumed that $O(7) = 0$. By using Equation (1) then at $Y_1 = 1.0$, Y_k should equal -0.00352. The actual ray traced point comes out at $Y_k = -0.0041$. This difference, 0.0006, is small compared to the total spherical aberration -0.0041. This means that the spherical aberration curve shown in Figure 8.5 may be approximately obtained by calculating the third order coefficient b_3 from axial paraxial ray data, and tracing one non-paraxial ray. On the other hand, the curve can also be obtained by tracing two non-paraxial rays, and calculating b_3 and b_5. Since the third order coefficient calculation depends on the individual surface contributions, it helps the designer see the source of the aberrations. For the example shown in Table 8.2, we see that the first two, and the last two surfaces of the lens give negative spherical aberration. The two surfaces of the central negative element provide all the positive or over-correction. The contribution on surface number four of the lens has the largest positive value. This coupled with the large angle of incidence on this surface is the main reason that the fifth order coefficient is positive. If one wanted to reduce the fifth order coefficient, it would be necessary to find a solution with a smaller angle of incidence on this surface or a smaller spherical aberration coefficient. If the fifth order coefficient were reduced, the total aberration (full curve) will be closer to the third order. The maximum under-correction, which now occurs at about $Y_1 = 1.1$, would increase and would occur at a larger Y_1. Such a lens would exhibit an increased zonal spherical aberration. The point of zero aberration, now at $Y_1 = 1.5$, would increase towards larger values of Y_1, so that the lens could be used at a larger aperture.

8.5.2.4 The Y_k versus Y_1 curves shown in Figure 8.5 were obtained in D light. Similar calculations could be made in F and C light. The value of b_3 can vary with wavelength, and since the plot is made for the paraxial focal plane in D light, the F and C paraxial rays will focus farther from the lens by approximately $f'/2200$. Therefore b_1 for F and C light, if we have a true (F - C) achromat, will be positive and equal to 1/2200. On this scale this is a negligible amount of aberration amounting to one-tenth of the zonal aberration, 0.0041. The F and C curves, corresponding to Figure 8.5, would have a positive slope at $Y_1 = 0$.

8.5.3 The Seidel spherical aberration.

8.5.3.1 Equations (3), (4) and (5) give the calculation of ${}_3Y_k$, the third order approximation to Y_k. Because $\bar{Y}_k = 0$, and hence for an unaberrated image point $Y_k = 0$, ${}_3Y_k$ is the third order approximation to the spherical aberration, measured in a plane perpendicular to the optical axis. Hence, it is sometimes referred to as the transverse spherical aberration. In the following section the aberrations of an off-axis image point will also be expressed as transverse aberrations.

8.5.3.2 Another measure of spherical aberration, called the longitudinal spherical aberration, is the distance along the optical axis between the paraxial image plane and the non-paraxial ray. The third order approximation to the longitudinal spherical aberration, referred to as the Seidel longitudinal spherical aberration, is numerically equal to ${}_3Y_k / u_{k-1}$. Hence, from an expression for the Seidel aberration, Equations (3), (4) and (5) readily follow.

8.6 IMAGERY FOR AN OFF-AXIS OBJECT POINT

8.6.1 The oblique image polynomial.

8.6.1.1 The solid curve in Figure 8.7 (a) is a plot of meridional rays traced through the sample lens at 10° ($K_o = 0$, $L_o = 0.1736$). The coordinates for the entering rays on the entrance pupil extend from $Y_1 = 1.35$ to $Y_1 = -1.35$. The vertical scale is again $(Y_k - \bar{Y}_k)$. The curve represents the displacement between the ray heights and the chief ray height in the paraxial image plane. This curve may also be represented by a power series. The power series can be expressed in different ways, but the following uses the well known Seidel third order coefficients. The polynomial can be expressed for any ray coordinate (Y_1, X_1) in the entrance pupil for any object height $\bar{Y}_o$ ($\bar{X}_o = 0$). Hence the series are sufficiently general so that they can be used with skew rays. There are two equations, one for $(Y_k - \bar{Y}_k)$,

and the other for X_k . $\overline{X}_k$ is always zero. These equations are

$$Y_k - \overline{Y}_k = - \frac{1}{2\,(n_{k-1}\,u_{k-1})} \left[\Sigma B\,(Y_1^2 + X_1^2)\,\frac{Y_1}{y_1^3} + \Sigma F\,\frac{3Y_1^2 + X_1^2}{y_1^2}\left(\frac{\overline{Y}_o}{\overline{y}_o}\right) + \Sigma(3C + P\Phi^2)\,\frac{Y_1}{y_1}\left(\frac{\overline{Y}_o}{\overline{y}_o}\right)^2 \right] + O(5), \qquad (6)$$

and

$$X_k = - \frac{1}{2\,(n_{k-1}\,u_{k-1})} \left[\Sigma B\,(Y_1^2 + X_1^2)\,\frac{X_1}{y_1^3} + \Sigma F\,\frac{(2Y_1\,X_1)}{y_1^2}\left(\frac{\overline{Y}_o}{\overline{y}_o}\right) + \Sigma(C + P\Phi^2)\left(\frac{X_1}{y_1}\right)\left(\frac{\overline{Y}_o}{\overline{y}_o}\right)^2 \right] + O(5)\,. \qquad (7)$$

8.6.1.2 The expressions ΣB , ΣF , ΣC and ΣP are the sums of the third order surface contributions for spherical aberration, coma, astigmatism and Petzval curvature. (C must not be confused with c , the curvature of a surface.) The terms, y_1 , $\overline{y}_o$, and $n_{k-1}\,u_{k-1}$, are the data from the two paraxial rays traced through the system. $\overline{Y}_o$ is the object point height. Y_1 and X_1 are coordinates for a general ray in the entrance pupil. If the object point is at infinity, as it is in the example being described, then $\overline{Y}_o / \overline{y}_o$ should be replaced by $(\tan \overline{U}_o)/\overline{u}_o$ or $L_o / M_o\,\overline{u}_o$.

8.6.1.3 If ΣB , ΣF , ΣC and ΣP are known, Equations (6) and (7) can be used to predict the position coordinates of any ray in the image surface corresponding to a given point in the object surface. The accuracy of the prediction depends on the magnitude of aberrations higher than third order. According to the first order theory, the chief ray should strike the image plane at $\overline{Y}_k = \overline{Y}_o\,m$ if $\overline{Y}_o$ is finite, or at $\overline{Y}_k = f \tan \overline{U}_o$, if the object is at infinity. However, the actual chief ray is displaced from the ideal image point due to a fifth aberration, distortion. There is also a polynomial to express this displacement.

$$(\overline{Y}_k - \overline{Y}_o\,m) = - \frac{\Sigma E}{2\,(n_{k-1}\,u_{k-1})} \left(\frac{\overline{Y}_o}{\overline{y}_o}\right)^3 + O(5)\,, \qquad (8)$$

where ΣE is the third order contribution for distortion. Equation (8) can be included in Equation (6) but it was not because it is somewhat easier to plot $(Y_k - \overline{Y}_k)$ as has been done in Figure 8.7. The fractional distortion which is defined by the ratio $(\overline{Y}_k - \overline{Y}_o\,m)/\overline{Y}_o\,m$ may be written to read as follows,

$$\text{fractional distortion} = \frac{\overline{Y}_k - \overline{Y}_o\,m}{\overline{Y}_o\,m} \doteq - \frac{\Sigma E}{2\,\Phi}\left(\frac{\overline{Y}_o}{\overline{y}_o}\right)^2 .$$

Note that the fractional distortion varies with the square of the object height ratio $(\overline{Y}_o/\overline{y}_o)$. In Section 8.7 the method for calculating B , F , C , E and P will be described. The actual calculations for the sample problem are shown in Table 8.2.

8.6.2 Examples of third order aberrations.

8.6.2.1 The third order ray predictions for $(Y_k - \overline{Y}_k)$ and X_k are shown by the dotted curves in Figures 8.5 , 8.7 and 8.8 . The solid curves show the actual coordinates for rays traced through the same entrance pupil points. Figures 8.7 (a), (b) and (c) are plots for fans of meridional rays at 10°, 15° and 20° respectively. Figures 8.8 (a) and 8.8 (b) show plots for skew fans with $Y_1 = 0$. Figure 8.9 is a plot of the fractional distortion of the lens as a function of the object field angle. The results show that the actual distortion is slightly more positive than predicted from the third order theory.

8.6.2.2 Finally in Figure 8.10 the slopes of all the curves at the chief ray are indicated. (Slopes are proportional to t_k). Curves of this type are called field curves. The points on the curves show the longitudinal distances from the paraxial image plane to the focus of rays close to the chief ray. The three third order field curves were found from surface contributions. The remaining two, the tangential field curve and the sagittal field curve, were obtained by graphically determining the slope of the meridional and skew ray plots respectively. These are shown in Figure 8.7, and in Figure 8.8. The third order tangential and sagittal field curves may be calculated by differentiating Equations (6) and (7) with respect to Y_1 and X_1

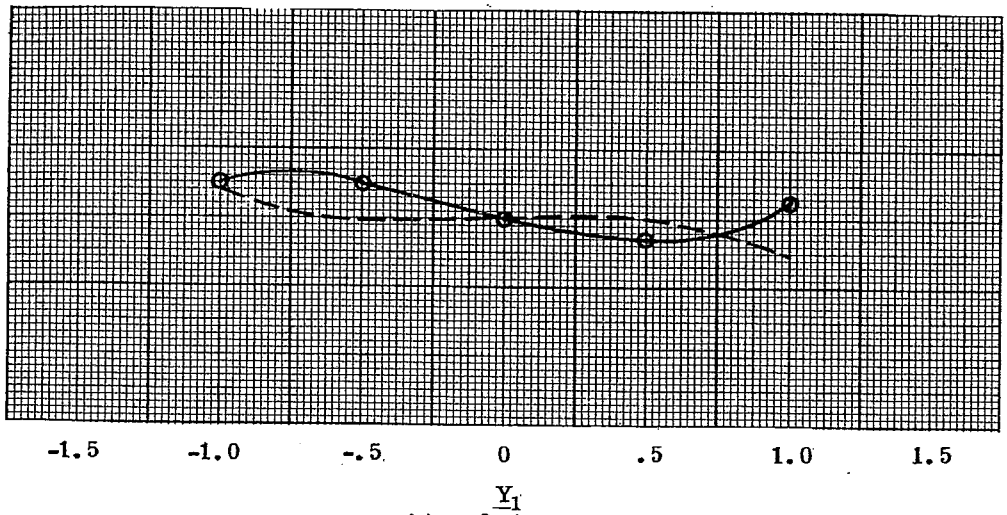

(c) 20° Obliquity

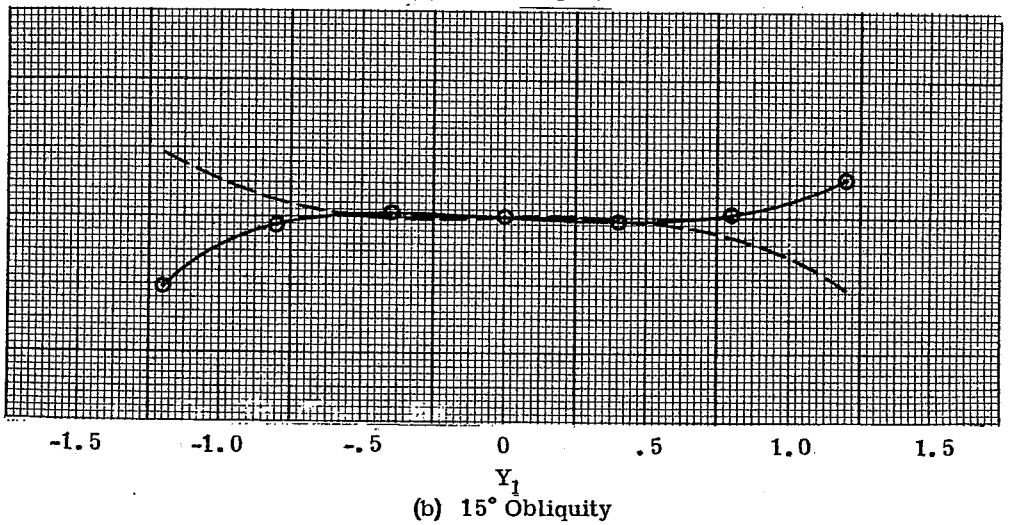

(b) 15° Obliquity

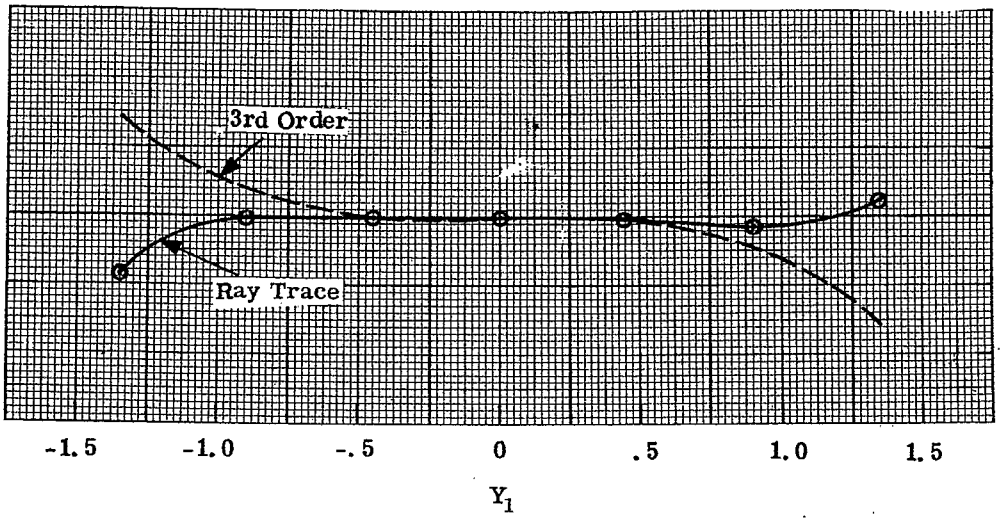

(a) 10° Obliquity

Figure 8.7 - Meridional ray plots.

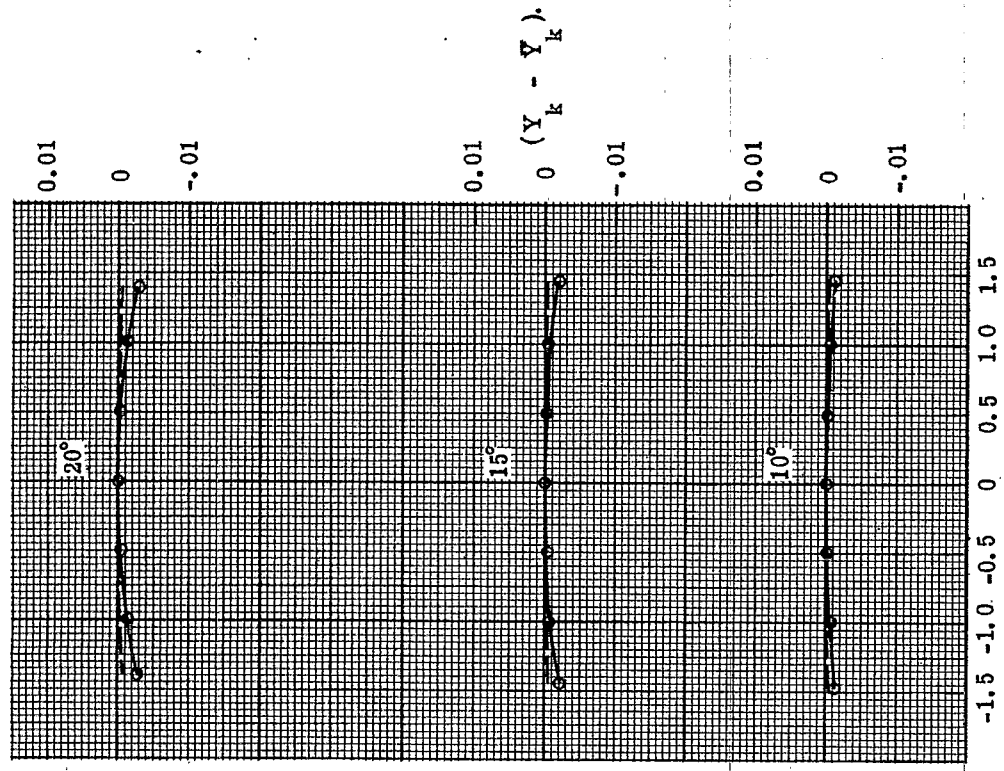

Figure 8.8 (b) - Skew ray image coordinates $(Y_k - \bar{Y}_k)$.

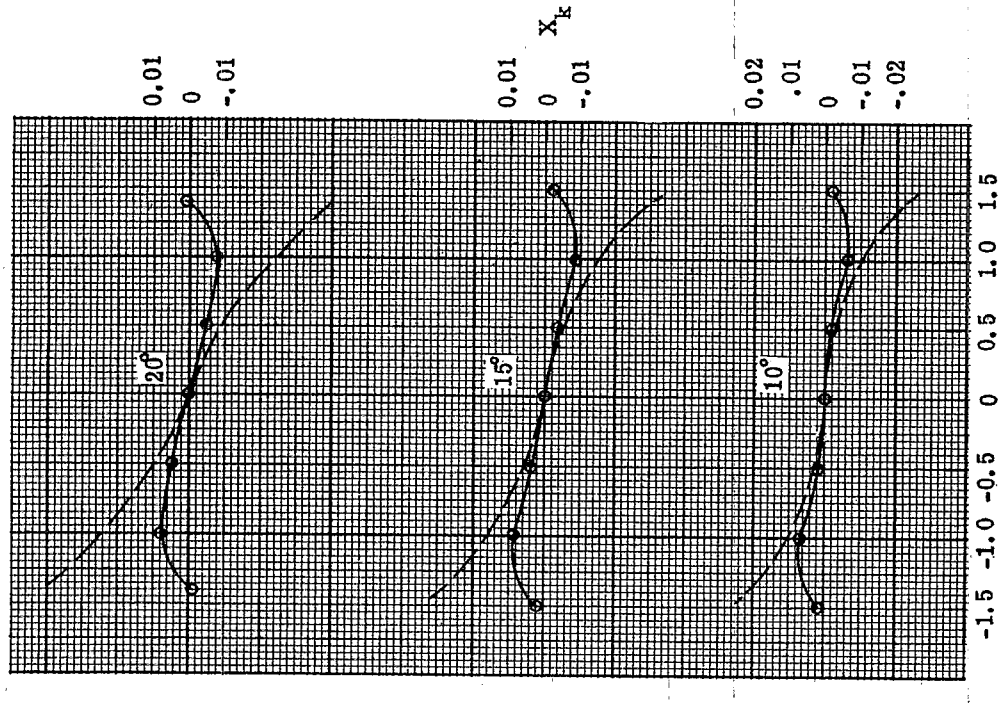

Figure 8.8 (a) - Skew ray image coordinates (X_k).

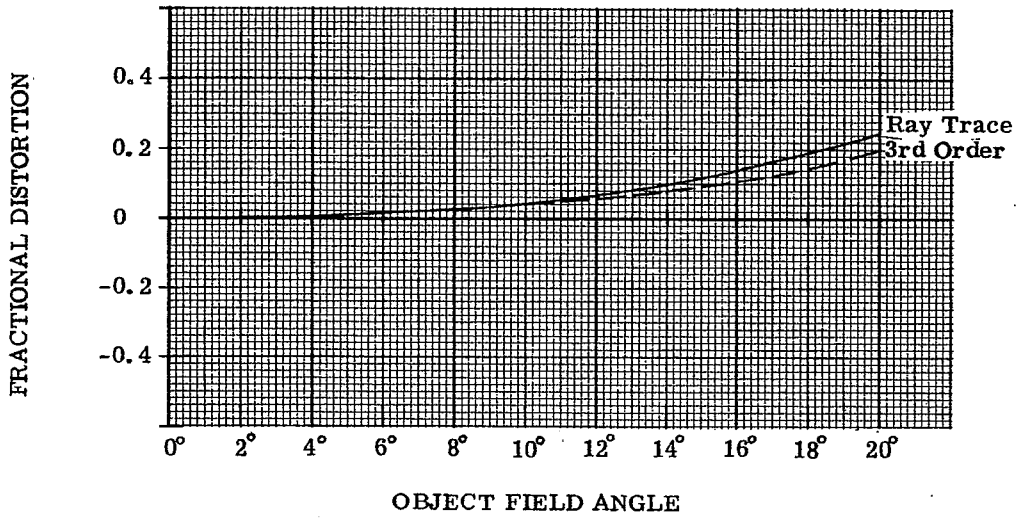

Figure 8.9 - Fractional distortion as a function of field angle.

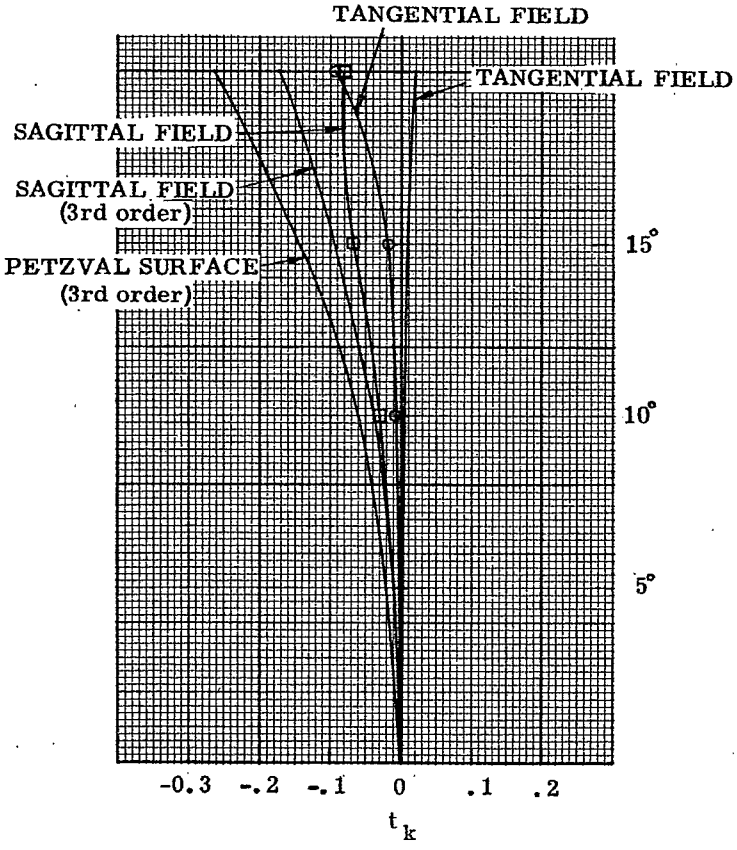

Figure 8.10 - Field curves for a triplet.

respectively and evaluating at $Y_1 = X_1 = 0$. The B and F terms drop out, leaving only the third terms. The final equation for the tangential fan is

$$t_{kT} = \frac{1}{2\,(n_{k-1}\,u_{k-1}{}^2)} \left[\Sigma\,(3C + P\Phi^2) \left(\frac{L_o}{M_o\,\bar{u}_o}\right)^2 \right]. \qquad (9)$$

For the sagittal fan, the equation is

$$t_{kS} = \frac{1}{2\,(n_{k-1}\,u_{k-1}{}^2)} \left[\Sigma\,(C + P\Phi^2) \left(\frac{L_o}{M_o\,\bar{u}_o}\right)^2 \right]. \qquad (10)$$

The Petzval surface curve is determined by the equation

$$t_{kP} = \frac{1}{2}\,(3t_{kS} - t_{kT}) = \frac{1}{2\,(n_{k-1}\,u_{k-1}{}^2)} \left[\Sigma P\Phi^2 \left(\frac{L_o}{M_o\,\bar{u}_o}\right)^2 \right].$$

Comparing this with Equation (9) and (10), it is clear that for $C = 0$, $t_{kP} = t_{kT} = t_{kS}$.

8.7 CALCULATION OF THE THIRD ORDER CONTRIBUTIONS B, F, C, E AND P

8.7.1 Basic formulae. The method for calculating B, surface by surface, was explained in Paragraph 8.5.2.2, and a sample calculation was given in Table 8.2. The coefficients F, C and E are calculated, surface by surface, by using the data of both the axial and chief paraxial rays. The formulae are:

$$B = S\,i^2 \qquad (4)$$

$$F = S\,i\,\bar{i} \qquad (11)$$

$$C = S\,\bar{i}^2 \qquad (12)$$

$$E = \bar{S}\,i\,\bar{i} + \Phi(\bar{u}_{-1}{}^2 - \bar{u}^2)\,*. \qquad (13)$$

P is calculated for each surface from the equation

$$P = \frac{c\,(n_{-1} - n)}{n_{-1}\,n}. \qquad (14)$$

As in the case of Equations (3), (4) and (5), Equations (6), (7), (8), (11), (12), (13) and (14) are derived from the Seidel expressions for coma, astigmatism, distortion and Petzval curvature.

8.7.2 Calculation of aberrations. These surface contributions have been worked out, surface by surface, in the sample problem shown in Table 8.2. The individual surface contributions, when summed up for all the surfaces, may be inserted in Equations (6) and (7) to evaluate the third order polynomials.

8.7.3 Fourth order aspheric effects. A fourth order aspheric deformation term on a surface introduces the following amounts of third order aberrations,

$$B = 8\,(n_{-1} - n)\,e\,y^4 \qquad (4a)$$

$$F = B\,\bar{y}/y \qquad (11a)$$

$$C = B\,(\bar{y}/y)^2 \qquad (12a)$$

$$E = B\,(\bar{y}/y)^3. \qquad (13a)$$

Note that the aspheric deformation term introduces aberrations independent of the curvature of the surface. It introduces no first order chromatic effects or Petzval contribution.

---

* $\bar{S}$ is calculated from Equation (5) using data from the chief ray.

8.7.4 The value of using third order aberration coefficients.

8.7.4.1 Inspection of the ray tracing data in Figures 8.5, 8.7 and 8.8 shows that the third order aberration polynomial does not predict the true aberration accurately for large apertures or field angles. However, third order aberration theory is extremely valuable. Even with present day computers, it is almost essential for a designer to calculate the third order aberrations of a system under consideration. Third order aberration theory provides target values for the designer; the third order aberrations must be within fairly narrow regions in order to obtain a satisfactory design. It is then up to the designer to find a layout which will lie within this third order region, but which will either balance or reduce the higher order aberrations.

8.7.4.2 Third order surface contributions provide the designer with a means for understanding a lens. He knows that the aberrations should be corrected with evenly balanced third order contributions. In other words, the third order contributions of a single aberration should be approximately equal numerically, but have alternating signs so that the sum is small. A large third order aberration on a surface will introduce a large higher order aberration of the same sign. Hence, the third order aberrations should be kept small. It is surprising how well one can control higher order aberrations through the use of third order calculations by remembering the following recommendations.

(1) Try to find the required third order solution with small, evenly distributed aberration contributions. It is seldom advisable to introduce a large contribution on one surface to cancel out several small ones due to other surfaces.

(2) Try to avoid large angles of incidence. The angle of incidence strongly affects the magnitude of higher order aberration contributions.

(3) If a given surface introduces a large amount of any third order aberration, try to correct this by another surface as nearby as possible. The reason for this is that a surface introducing large amounts of third order aberrations also introduces a series of higher order aberrations. If the third order aberrations are corrected by a neighboring surface, the higher order aberrations tend to cancel one another, but if correction is done at some other part of the optical system, the higher order aberrations will not necessarily cancel. For example, if a large amount of spherical aberration is introduced at a position in the system where $\bar{y}/y = k$, then this aberration should be corrected at a surface as close as possible to the position where $\bar{y}/y = k$. It may often be impossible, in a given design, to make the ideal correction, but it is an important step in design procedure to make the attempt. One of the main reasons that aspheric surfaces are so valuable, is that they do allow the introduction of aberration at nearly any place in the optical system, without upsetting the distribution of focal lengths of the different elements needed to correct for color and Petzval field curvature.

8.8 AFOCAL OPTICAL SYSTEMS

8.8.1 Third order polynomial. In telescopic systems, where both the object and image are at infinity, it is convenient to plot the tangents of the angles which the emerging rays make with the optical axis, versus the coordinates (X_1, Y_1) of the entering rays. The meridional ray $(X_1 = 0$ and Y_1 arbitrary$)$ data are plotted as $\left(\frac{L_{k-1}}{M_{k-1}} - \frac{\bar{L}_{k-1}}{\bar{M}_{k-1}}\right)$ versus Y_1. The skew ray $(Y_1 = 0$ and X_1 arbitrary$)$ data are plotted as two curves:

$$\frac{K_{k-1}}{M_{k-1}} \quad \text{versus} \quad X_1 ,$$

and

$$\left(\frac{L_{k-1}}{M_{k-1}} - \frac{\bar{L}_{k-1}}{\bar{M}_{k-1}}\right) \quad \text{versus} \quad X_1 .$$

The third order polynomial may then be written as in Equations (6) and (7) by making the following substitutions:

$$Y_k = -\frac{y_{k-1}}{u_{k-1}} \tan U_{k-1} \qquad X_k = -\frac{y_{k-1}}{u_{k-1}} \frac{K_{k-1}}{M_{k-1}}$$

and

$$\bar{Y}_k = -\frac{y_{k-1}}{u_{k-1}} \tan \bar{U}_{k-1} .$$

Equations (6) and (7) then become

$$\left(\frac{L_{k-1}}{M_{k-1}} - \frac{\bar{L}_{k-1}}{\bar{M}_{k-1}}\right) = \frac{1}{2(n_{k-1}\, y_{k-1})}\left[\Sigma B\,(Y_1^2 + X_1^2)\,\frac{Y_1}{y_1^3} + \Sigma F\,\frac{(3Y_1^2 + X_1^2)}{y_1^2}\left(\frac{\bar{Y}_o}{\bar{y}_o}\right)\right.$$

$$\left. + \Sigma(3C + P\Phi^2)\,\frac{Y_1}{y_1}\left(\frac{\bar{Y}_o}{\bar{y}_o}\right)^2\right] + O(5)\,, \qquad (15)$$

and

$$\frac{K_{k-1}}{M_{k-1}} = \frac{1}{2(n_{k-1}\, y_{k-1})}\left[\Sigma B\,(Y_1^2 + X_1^2)\left(\frac{X_1}{y_1^3}\right) + \Sigma F\,\frac{(2\,Y_1\,X_1)}{y_1^2}\left(\frac{\bar{Y}_o}{\bar{y}_o}\right)\right.$$

$$\left. + \Sigma(C + P\Phi^2)\left(\frac{X_1}{y_1}\right)\left(\frac{\bar{Y}_o}{\bar{y}_o}\right)^2\right] + O(5)\,. \qquad (16)$$

8.8.2 Spot diagram.

8.8.2.1 In an ideal, aberration-free afocal system, the emergent rays from the $k - 1$ surface are parallel. In a real afocal system these rays are almost parallel. The intersection of these rays with a plane would give a series of points more or less evenly spaced; the points would not be concentrated, as in a spot diagram (see Figure 8.1 (b)), and it would be difficult to interpret the diagram in the same way as in the case of the spot diagram.

8.8.2.2 It is possible to concentrate these almost parallel emergent rays and make a spot diagram for an afocal system by adding a hypothetical aberration-free thin lens at the rear of the system with any desired focal length. This is effectively done simply by changing the coordinates for each ray on the last surface of the system to zero. The rays then proceed to the final focal plane of the aberration-free lens from this point at the same angles because they pass through the center (coinciding nodal points) of the thin lens. The distance to the image plane is the arbitrary focal length of this lens. The spread of the points from a single, concentrated spot, is an indication of the non-parallelism of the emergent rays. This in turn is an indication of the aberrations of the afocal system.

8.9 STOP SHIFT EQUATIONS

8.9.1 General. The aim of a lens designer is to minimize the aberrations of the optical system within the specifications of f - number and field of view. It is clear by Equations (4), (5), (11), (12), (13) and (14) that the third order coefficients depend on index, curvature, and thickness. By Equations 6-(34) and 6-(35), the first order chromatic coefficients also depend on these parameters. But the occurrence of $\bar{i}$, $\bar{S}$, and $\bar{u}_{-1}$, in Equations (11), (12), (13) and 6-(35), show that the oblique aberrations (coma, astigmatism, distortion, and lateral color) depend on the position of the aperture stop as well. Hence it is necessary for the designer to know the effect of the stop position on these aberrations.

8.9.2 Aberration polynomial for a shifted chief ray.

8.9.2.1 The aberration polynomials shown in Equations (6) and (7) are calculated from the coefficients B, F, C and E which are determined by tracing an axial and an oblique chief paraxial ray. It is possible to compute the aberration polynomial for any other paraxial chief ray. The term other paraxial chief ray, or shifted chief ray, refers to another ray which crosses the optical axis at the new pupil points. Hence shifting the aperture stop results in a new ray becoming the (shifted) chief ray. Suppose we wish to write down the aberration polynomial for a paraxial chief ray which passes through the original entrance pupil at a height of $\bar{y}^*$. A ray from object point $\bar{Y}_o$ passing through the original entrance pupil at a height of Y_1 will be at a height of Y_1' in the original entrance pupil above the new chief ray. Figure 8.11 shows that $Y_1 = Y_1' + \bar{Y}_1^*$.

8.9.2.2 Equation (6) may be written now in terms of Y_1'. The distortion term in Equation (8) is added to Equation (6) to give the aberration $Y_k - \bar{Y}_o\, m$. For an object of height $\bar{Y}_o$, it can be seen by similar triangles that $\bar{Y}_1^*$ is given by

$$\bar{Y}_1^* = \bar{y}_1^*\left(\frac{\bar{Y}_o}{\bar{y}_o}\right).$$

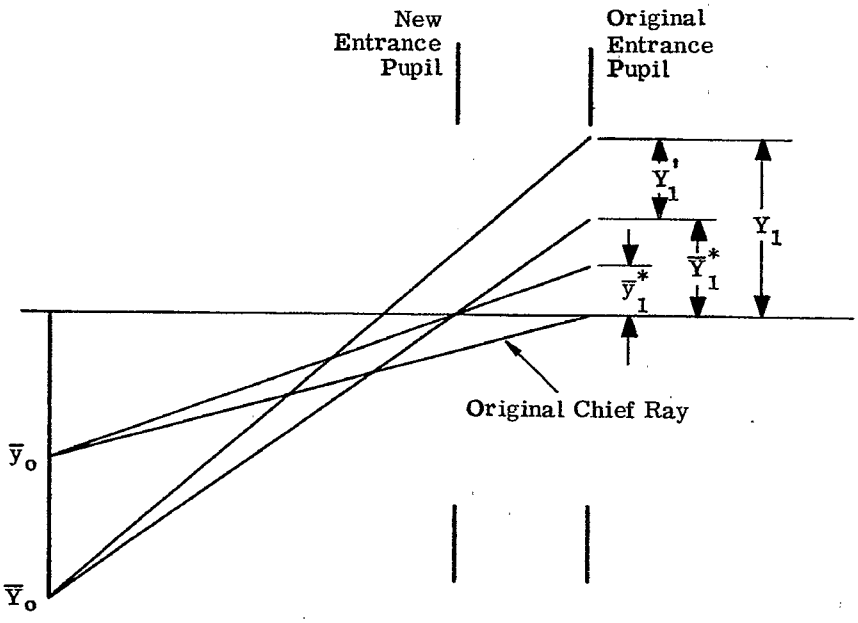

Figure 8.11 - Application of stop shift equations.

Then the height Y_1' of the ray above the new chief ray is

$$Y_1' = Y_1 - \bar{Y}_1^* = Y_1 - \bar{y}_1^* \left(\frac{\bar{Y}_o}{\bar{y}_o}\right) .$$

By substituting this expression into the sum of Equations (6) and (8), and by using the relation,

$$Q = \bar{y}_1^* / y_1 ,$$

it is possible to arrive at the equation

$$(Y_k - \bar{Y}_o\, m) = -\frac{1}{2(n_{k-1}\, u_{k-1})} \left[\Sigma B (Y_1'^2 + X_1^2) \left(\frac{Y_1'}{y_1^3}\right) + (Q\Sigma B + \Sigma F)\left(\frac{3Y_1'^2 + X_1^2}{y_1^2}\right)\left(\frac{\bar{Y}_o}{\bar{y}_o}\right) + \right.$$

$$\left[3Q^2\Sigma B + 6Q\,\Sigma F + \Sigma(3C + P\Phi^2)\right] \left(\frac{Y_1'}{y_1}\right) \left(\frac{\bar{Y}_o}{\bar{y}_o}\right)^2 +$$

$$\left. \left[Q^3\Sigma B + 3Q^2\Sigma F + Q\Sigma(3C + P\Phi^2) + \Sigma E\right]\left(\frac{\bar{Y}_o}{\bar{y}_o}\right)^3 \right] . \qquad (17)$$

8.9.3 Third order aberration coefficients. Equation (17) is the aberration polynomial with a shifted chief ray and therefore a shifted entrance pupil. If this equation is compared with the sum of Equations (6) and (8) it has a similar form. In Equation (17) the original aberration coefficients ΣB, ΣF, ΣC, ΣE and ΣP have been replaced by linear combinations of these coefficients. Since the aberration polynomial has the same form it can be said that the third order coefficients have changed to new values. The new third order coefficients will be indicated with a superscript *. By comparing Equation (17) with Equations

(6) and (8) it follows that

$$\Sigma B^* = \Sigma B , \tag{18}$$

$$\Sigma F^* = Q\Sigma B + \Sigma F , \tag{19}$$

$$\Sigma C^* = Q^2 \Sigma B + 2Q\Sigma F + \Sigma C , \tag{20}$$

$$\Sigma E^* = Q^3 \Sigma B + 3Q^2 \Sigma F + Q\Sigma(3C + P\Phi^2) + \Sigma E , \tag{21}$$

and

$$\Sigma P^* = \Sigma P . \tag{21a}$$

8.9.4 First order aberration coefficients. Using Equation 6-(39), to complete the list of changes of the aberration coefficients as the chief ray is changed, the chromatic coefficients then become

$$a^* = a , \tag{22}$$

and

$$b^* = Q a + b . \tag{23}$$

8.9.5 Use of the stop shift equations.

8.9.5.1 These equations, (18-23), are often called the stop shift equations. They are extremely useful and will be referred to many times in later sections. They enable the designer to predict how the third order coefficients change with the choice of the chief ray. Again we see that any two paraxial rays traced through the lens are sufficient for all third order calculations on the system. If the oblique chief ray traced through the system turns out not to pass through the center of the new aperture stop, it is possible to use the stop shift formulae to compute the third order coefficients for the chief ray that does pass through.

8.9.5.2 The designer should note that Equation (17) uses the aperture variable Y_1' . As shown in Figure 8.11, Y_1' is the height of a general ray above the new chief ray in the original entrance pupil. The height of this general ray above the chief ray in the new entrance pupil will not be Y_1' if the object is at a finite distance. In order to write the polynomial in terms of Y_1 one must account for the magnification between the original and the new entrance pupil. Now it should be noted that the polynomial involves the ratio of Y_1' / y_1 . It turns out that the corresponding ratio for the new entrance pupil has the same value. Therefore the aberration polynomial, Equation (17), can be used with Y_1' and y_1 as coordinates in the new entrance pupil.

8.10 THIN LENS ABERRATION THEORY

8.10.1 Third order coefficients. It is possible to combine the two surface contributions of a thin lens in air and obtain simple expressions for the third order aberrations. By assuming that the lens is thin, the values of y for the axial paraxial ray are the same on the two surfaces. If it is further assumed that the lens is the aperture stop (and hence the entrance and exit pupils), the oblique paraxial chief ray passes through the center of the thin lens at $\bar{y} = 0$. The third order aberration coefficients of the thin lens are then

$$B = \alpha_1 + \alpha_2 c_1 + \alpha_3 c_1^2 , \tag{24}$$

$$F = \beta_1 + \beta_2 c_1 , \tag{25}$$

$$C = -\phi\Phi^2 , \tag{26}$$

$$E = 0 , \tag{27}$$

and

$$P = -\frac{\phi}{n} . \tag{28}$$

The constants of the new equations are:

$$\alpha_1 = -\frac{\phi y^4}{n}\left[(3n+2)\left(\frac{u_{-1}}{y}\right)^2 + \left(\frac{\phi n}{n-1}\right)^2 n - \frac{\phi n}{n-1}(3n+1)\frac{u_{-1}}{y}\right], \quad (29)$$

$$\alpha_2 = -\frac{\phi y^4}{n}\left[(4n+4)\left(\frac{u_{-1}}{y}\right) - \left(\frac{\phi n}{n-1}\right)(2n+1)\right], \quad (30)$$

$$\alpha_3 = -\frac{\phi y^4}{n}(n+2), \quad (31)$$

$$\beta_1 = \frac{\phi \Phi y^2}{n}\left[(2n+1)\frac{u_{-1}}{y} - \left(\frac{\phi n}{n-1}\right) n\right], \quad (32)$$

$$\beta_2 = \frac{\phi \Phi y^2}{n}(n+1), \quad (33)$$

$$\phi = \frac{(u_{-1} - u)}{y} = \frac{1}{f} \text{ (from Equation 6-(24))}, \quad (34)$$

and

$$\Phi = \bar{y}\, u_{-1} - y\, \bar{u}_{-1} = \bar{y} u - y \bar{u}, \quad (35)$$

where u_{-1} is the angle of the axial paraxial ray in air on the left hand side of the thin lens and u is the angle of this ray in air on the right hand side, n is the index of the lens, and c_1 is the curvature of the first surface.

8.10.2 Limitations; comparison with thick lens results.

8.10.2.1 Equations (24) through (28) are valid for any thin lens in air at any position in a system provided $\bar{y} = 0$ at the lens. If the value of $\bar{y}$ is not zero it is necessary to calculate B^*, F^*, C^*, E^*, and P^* from the stop shift equations (18) through (21a). With the proper substitution it can be shown that,

$$B^* = \alpha_1^* + \alpha_2^* c_1 + \alpha_3^* c_1^2, \quad (36)$$

$$F^* = \beta_1^* + \beta_2^* c_1 + \beta_3^* c_1^2, \quad (37)$$

$$C^* = \gamma_1^* + \gamma_2^* c_1 + \gamma_3^* c_1^2, \quad (38)$$

$$E^* = \delta_1^* + \delta_2^* c_1 + \delta_3^* c_1^2. \quad (39)$$

The coefficients of these quadratic equations are as follows:

$$\alpha_1^* = \alpha_1, \quad \alpha_2^* = \alpha_2, \quad \alpha_3^* = \alpha_3, \quad (40)$$

$$\beta_1^* = Q q_1 + \beta_1, \quad (41)$$

$$\beta_2^* = Q q_2 + \beta_2, \quad (42)$$

$$\beta_3^* = Q \alpha_3, \quad (43)$$

$$\gamma_1^* = Q^2 \alpha_1 + 2Q \beta_1 - \phi \Phi^2, \quad (44)$$

$$\gamma_2^* = Q^2 \alpha_2 + 2Q \beta_2, \quad (45)$$

$$\gamma_3^* = Q^2 q_3, \quad (46)$$

$$\delta_1^* = Q^3 \alpha_1 + 3Q^2 \beta_1 - Q(3n+1)\frac{\phi \Phi^2}{n}, \quad (47)$$

$$\delta_2^* = Q^3 \alpha_2 + 3Q^2 \beta_2, \quad (48)$$

and

$$\delta_3^* = Q^3 \alpha_3. \quad (49)$$

8.10.2.2 To illustrate the use of these equations a sample calculation for all the thin lens coefficients is presented in Table 8.4. In this example, the calculations were made on the thin lens illustrated in Table 6.13. Table 8.2 shows the same lens system with thickness added. The thin lens equations were used with

$c_1 = 0.253$ for lens (a),

$c_1 = -0.200$ for lens (b),

and

$c_1 = 0.050$ for lens (c).

8.10.2.3 Table 8.3 lists a comparison between the third order aberration coefficients calculated from the thin lens equations and those calculated from the surface contributions of the thick lens. The differences between the coefficients is due to the thicknesses introduced in the sample shown in Table 8.2. Slight differences are also due to the differences in c_1.

8.10.2.4 In the following sections it will be demonstrated how the thin lens equations are used in the preliminary design of a lens system.

Lens and Coefficient		Thin Lens Formula	Thick Lens Formula
Lens (a) $C_1 = 0.253$	B	-0.0365	-0.0355
	F	0.0241	0.0221
	C	-0.0647	-0.0604
	E	0.1046	0.0962
	P	-0.1021	-0.1024
Lens (b) $C_1 = -0.200$	B	0.0722	0.0731
	F	-0.0340	-0.0352
	C	0.0895	0.0919
	E	-0.0182	-0.0195
	P	0.1770	0.1759
Lens (c) $C_1 = 0.050$	B	-0.0443	-0.0440
	F	0.0136	0.1029
	C	-0.0290	-0.0272
	E	-0.0776	-0.0746
	P	-0.1124	-0.1135

Table 8.3 - Comparison between third order aberrations calculated from thin lens equations and from individual surface contributions of a thick lens.

Quantity	Lens (a)	Lens (b)	Lens (c)
y^2	2.25000	1.28989	1.56630
y^4	5.06250	1.66380	2.45329
$-\phi y^4/n$	-0.51678	0.29456	-0.27574
$\phi\Phi$	-0.09029	0.15669	-0.09942
$\phi\Phi y^2/n$	-0.12541	0.12468	-0.09612
$-\phi\Phi^2$	-0.04930	0.08555	-0.05428
n+1	2.6200	2.6210	2.6200
n+2	3.6200	3.6210	3.6200
2n+1	4.2400	4.2420	4.2400
3n+1	5.8600	5.8630	5.8600
3n+2	6.8600	6.8630	6.8600
4n+4	10.4800	10.4840	10.4800
u_{-1}/y	0	-0.21841	0.06223
$\phi n/n-1$	0.43210	-0.74911	0.47576
$(3n+2)\left(\frac{u_{-1}}{y}\right)^2$	0	0.32739	0.02656
$\left(\frac{\phi n}{n-1}\right)^2 n$	0.30246	0.90964	0.36668
$-\frac{\phi n}{n-1}(3n+1)\frac{u_{-1}}{y}$	0	-0.95926	-0.17348
α_1	-0.15631	0.08182	-0.06060
$(4n+4)\frac{u_{-1}}{y}$	0	-2.28981	0.65213
$-\frac{\phi n}{n-1}(2n+1)$	-1.83209	3.17771	-2.01721
α_2	0.94679	0.26153	0.37641
α_3	-1.87075	1.06659	-0.99817
$(2n+1)u_{-1}/y$	0	-0.92650	0.26384
$-\left(\frac{\phi n}{n-1}\right)n$	-0.70000	1.21430	-0.77073
β_1	0.08778	0.03588	0.04872
β_2	-0.32856	0.32680	-0.25183
Q	-0.53333	-0.06268	0.50844
β_1^*	0.17115	0.03076	0.01791
β_2^*	-0.83352	0.31040	-0.06045
β_3^*	0.99773	-0.06686	-0.50752
γ_1^*	-0.18740	0.08138	-0.02040
γ_2^*	0.61978	-0.03994	-0.15878
γ_3^*	-0.53212	0.00419	-0.25804
δ_1^*	0.19373	-0.01899	-0.07001
δ_2^*	-0.42400	-0.00379	-0.14584
δ_3^*	0.28380	-0.00026	-0.13120

Table 8.4 - Calculation of the thin lens coefficients for the thin lens shown in Table 6.13.